Structure and mechanism of the phage T4 recombination mediator protein UvsY

Stefan Gajewski[a], Michael Brett Waddell[a], Sivaraja Vaithiyalingam[a], Amanda Nourse[a], Zhenmei Li[a], Nils Woetzel[b,1], Nathan Alexander[b,2], Jens Meiler[b], and Stephen W. White[a,c,3]

[a]Department of Structural Biology, St. Jude Children's Research Hospital, Memphis, TN 38105; [b]Departments of Chemistry, Pharmacology, and Biomedical Informatics, Vanderbilt University, Nashville, TN 37232; and [c]Department of Microbiology, Immunology and Biochemistry, University of Tennessee Health Science Center, Memphis, TN 38163

Edited by Scott W. Morrical, University of Vermont, Burlington, VT, and accepted by the Editorial Board February 8, 2016 (received for review September 25, 2015)

The UvsY recombination mediator protein is critical for efficient homologous recombination in bacteriophage T4 and is the functional analog of the eukaryotic Rad52 protein. During T4 homologous recombination, the UvsX recombinase has to compete with the prebound gp32 single-stranded binding protein for DNA-binding sites and UvsY stimulates this filament nucleation event. We report here the crystal structure of UvsY in four similar open-barrel heptameric assemblies and provide structural and biophysical insights into its function. The UvsY heptamer was confirmed in solution by centrifugation and light scattering, and thermodynamic analyses revealed that the UvsY–ssDNA interaction occurs within the assembly via two distinct binding modes. Using surface plasmon resonance, we also examined the binding of UvsY to both ssDNA and the ssDNA–gp32 complex. These analyses confirmed that ssDNA can bind UvsY and gp32 independently and also as a ternary complex. They also showed that residues located on the rim of the heptamer are required for optimal binding to ssDNA, thus identifying the putative ssDNA-binding surface. We propose a model in which UvsY promotes a helical ssDNA conformation that disfavors the binding of gp32 and initiates the assembly of the ssDNA–UvsX filament.

homologous recombination | structural modification | DNA binding | DNA architecture | crystallography

Homologous recombination (HR) involves the exchange of strands between homologous DNA molecules and has fundamental roles in double-stranded DNA (dsDNA) break repair, the rescue of stalled replication forks, and recombination-dependent replication (1). Defects in HR are associated with genetic instability, chromosomal abnormalities, and cancer (1). HR is performed by an ATP-dependent recombinase, RecA in prokaryotes and Rad51 in eukaryotes, that creates a filament with approximately sixfold helical symmetry. The filament first binds single-stranded DNA (ssDNA) and then samples incoming dsDNA to search for homology and promote the exchange reaction (2, 3). Key insights into the mechanism have been provided by structural (4) and dynamics (5, 6) studies of the HR filament. ssDNA-binding proteins, RPA in eukaryotes and SSB in prokaryotes, protect the ssDNA from nucleases and remove secondary structures during HR, but they also block the binding of the recombinase (3). This obstacle is overcome by the recombination mediator proteins (RMPs) (7), Rad52 in eukaryotes and RecOR in prokaryotes, that stimulate the exchange of the ssDNA-binding proteins for the recombinase.

Phage T4 is able to process DNA in isolation from the host *Escherichia coli* by encoding all of the necessary DNA metabolic proteins. The T4 UvsXYW system encodes the core HR machinery (8) comprising UvsX (the recombinase), UvsW (the SF2 remodeling helicase), and UvsY (the RMP). Together with the T4 ssDNA-binding protein gp32 (9, 10), these three proteins can efficiently perform HR in an in vitro reconstituted system (11). UvsY is a 15.8-kDa protein with properties that are consistent with its role as an RMP; it stimulates the DNA-dependent ATPase activity of UvsX, lowers the critical concentration of UvsX that is required for activity, and promotes strand exchange (12–14). UvsY efficiently promotes the UvsX-catalyzed strand invasion reaction, and a model has been proposed in which UvsY is specifically recruited to ssDNA–gp32 complexes, promotes the release of gp32, and favors the binding of UvsX (12, 13, 15). Observed binary and ternary complexes among ssDNA, gp32, UvsY, and UvsX are consistent with this model (12, 13, 16–18). The functional association between UvsX and UvsY is reflected by the similar recombination defective phenotypes displayed in *uvsX*$^{-}$ and *uvsY*$^{-}$ mutants (19).

With the goal of understanding the mechanism of the HR machinery by using the phage T4 model system, we and others have determined the crystal structures of gp32 (10), UvsW (20), and UvsX (11). Here, we report the crystal structure of UvsY and show that it adopts a heptameric open-barrel assembly in which the putative ssDNA-binding surface extends along one edge. The structure is fully consistent with data from solution studies. Together with binding data from surface plasmon resonance (SPR) and isothermal titration calorimetry (ITC), we suggest that UvsY promotes the handover of gp32 for UvsX on ssDNA by modifying the architecture of the ssDNA–gp32 complex.

Significance

UvsY is the phage T4 recombination mediator protein, and structural and biophysical studies provide insights into its role in T4 homologous recombination. Homologous recombination mediates the error-free repair of DNA double-strand breaks and is found in all kingdoms of life. It is the mechanism whereby single-stranded DNA invades homologous double-stranded DNA to seek matching base pairs and then promotes strand exchange prior to DNA repair via recombination-dependent replication. Recombination is mediated by a recombinase that initially competes with single-strand DNA-binding proteins for access to the DNA. The role of the mediator proteins is to facilitate this handover. UvsY represents a model for how this exchange occurs in phage T4 that is directly applicable to higher organisms including humans.

Author contributions: S.G. designed research; S.G., M.B.W., S.V., A.N., and Z.L. performed research; N.W. and N.A. contributed new reagents/analytic tools; S.G., M.B.W., S.V., A.N., N.W., N.A., J.M., and S.W.W. analyzed data; and S.G., J.M., and S.W.W. wrote the paper.

The authors declare no conflict of interest.

This article is a PNAS Direct Submission. S.W.M. is a guest editor invited by the Editorial Board.

Freely available online through the PNAS open access option.

Data deposition: The atomic coordinates and structure factors have been deposited in the Protein Data Bank, www.pdb.org (PDB ID codes 4ZWQ, 4ZWR, 4ZWS, and 4ZWT).

[1]Present address: Heidelberg Institute for Theoretical Studies, 69118 Heidelberg, Germany.

[2]Present address: Department of Pharmacology, Case Western Reserve University, Cleveland, OH 44106.

[3]To whom correspondence should be addressed. Email: stephen.white@stjude.org.

This article contains supporting information online at www.pnas.org/lookup/suppl/doi:10.1073/pnas.1519154113/-/DCSupplemental.

Results

Crystallization and Structure Determination. Crystals of UvsY that diffract to 2.3 Å (type 1) were readily obtained, but they displayed severe diffraction anisotropy, and apparent pseudotranslational symmetry and possibly pseudocentering. Crystals with similar pathologies have been reported (21). We used reductive methylation (22) to obtain alternative crystals, and the modified UvsY produced a crystal form (type 2) in space group $C222_1$ that diffracted to 3.4 Å. These crystals had no apparent pathology apart from anisotropic diffraction, and selenomethionine-substituted (Se-Met) crystals generated an initial 5.4-Å electron density map with clear α-helices (*SI Appendix*, Table S1). Using BCL::EM_Fold (23), we built an initial α-helical backbone into the map and then expanded this backbone to a full atomic model with Rosetta (24) (*SI Appendix*, Fig. S1). The structure revealed an open heptameric assembly of α-helical UvsY protomers. Using this model, we successfully solved and refined the higher resolution type 1 structure in space group $C222_1$ with twin law -k, -h, -l and a twin fraction of 0.5. A third crystal form (type 3) was subsequently obtained from the unmodified UvsY in the presence of a dA3 oligonucleotide and refined to 2.6 Å. There was no obvious electron density for the ssDNA, and significant regions were missing from the map. However, it was possible to extrapolate a hybrid model of the complete type 3 structure, and this model revealed a more open heptameric assembly compared with the type 1 structure. A fourth crystal form (type 4) was grown from UvsY that was both methylated and mutated (E79A, K80A, S81A) to further reduce the potential negative effects on crystallization of surface residues. These I422 crystals diffracted poorly, but the structure clearly revealed a more condensed heptameric assembly compared with the type 1 structure. The heptameric UvsY assemblies revealed by the four crystal forms are shown in *SI Appendix*, Fig. S2, and data collection and refinement statistics are shown in *SI Appendix*, Table S2.

Verification of the UvsY Heptameric Assembly. To verify that the UvsY heptamer exists in solution, we performed analytical ultracentrifugation (AUC) and light scattering analyses. The AUC experiments included both sedimentation velocity and equilibrium analyses, and returned masses of 109,378 ± 430 Da and 108,904 ± 1,747 Da, respectively (*SI Appendix*, Fig. S3 *A* and *B*). A size exclusion chromatography coupled to multiangle light scattering (SEC-MALS) analysis yielded a mass estimate of 111,900 ± 280 Da (*SI Appendix*, Fig. S3*C*). These measurements are in close agreement with the theoretical mass (110,874 Da) of a UvsY heptamer.

The Structure of the UvsY Protomer. This description of the structure is based on the type 1 crystal form. The UvsY protomer is mostly α-helical with two long α-helices (helix H2, residues 21–65; helix H4, residues 90–134) forming an antiparallel coiled coil, and two shorter α-helices (helix H1, residues 2–14; helix H3, residues 80–89) packed against them. Loop L1 (residues 15–20) connects H1 and H2, and loop L2 (residues 66–79) connects H2 and H3. Fig. 1*A* shows the secondary structure within the UvsY sequence, and Fig. 1*B* shows the structure of the UvsY protomer with key residues highlighted. This helical assembly is stabilized by seven conserved intramolecular salt bridges: Glu9:Lys38, Asp13:Lys34, Glu24:Arg120, Lys53:Asp97, Glu45:Arg48, Glu50:Lys54, and Lys125:Asp129 (Fig. 1*B*). Although the side chains are not fully visible in the electron density map in some of the protomers, the latter three are apparently helix stabilizing "stapling" salt bridges. In addition, the four conserved aromatic residues Trp35, Tyr102, Trp103, and Phe109 are strategically located to provide key packing and hydrogen bonding interactions (Fig. 1*B*). At the "bottom" of the protomer, H1 and L1 bend back to associate with the H2/H4 coiled coil.

The H2/H4 interaction is offset by two turns such that residues 21–56 of H2 are packed against residues 92–127 of H4. The free C terminus of H2 engages L2 and H3 at the "top" of the structure and, together with the N terminus of H4, form an L2/H3 subdomain.

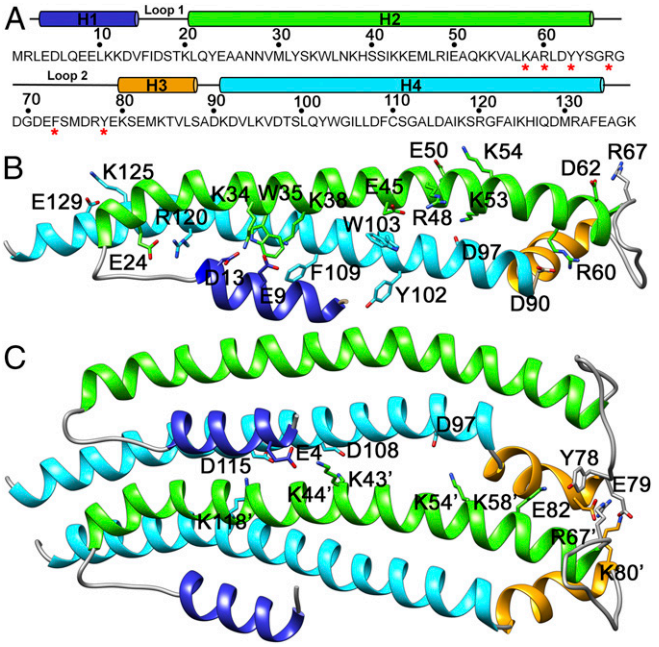

Fig. 1. Structural overview of the UvsY protomer and the protomer–protomer interactions. (*A*) The primary structure of UvsY with the four α-helical secondary structures labeled and individually colored. Residues mutated in the study are marked with a red asterisk. (*B*) Ribbon representation of UvsY with the same coloring scheme as *A*. Intramolecular salt bridges and structurally important aromatic residues are shown. (*C*) The interface between adjacent protomers in the heptameric assembly showing the interfacial salt bridges. Note that all of the acidic residues reside on one protomer and their partner basic residues are on the adjacent protomer (indicated by the prime after the residue number).

Within this subdomain, the adjacent Tyr63 and Tyr64 create a local hydrophobic core and mediate key interactions. These residues are well conserved in T4-like UvsY sequences, and a close up of their interactions within the L2/H3 subdomain is shown in Fig. 2*A*, and as stereoview together with the electron density in *SI Appendix*, Fig. S4. It should be noted that crystal forms 1, 2, and 4 all involve head-to-head crystal lattice packing interactions that are mediated by the L2/H3 subdomain, and although its conformation is somewhat variable, it retains these key structural features. Phe73, Met75, and Arg77 within the L2/H3 subdomain feature prominently in the head-to-head crystal packing, and the R77A mutant failed to crystallize. In crystal form 3, where there are minimal head-to-head packing interactions, the L2/H3 region is not visible, suggesting flexibility and/or the need for a binding partner for stability.

The UvsY Heptameric Assembly. The UvsY protomers assemble into an open-barrel heptameric assembly in which each protomer A to G packs in a parallel fashion with its neighbors (Fig. 3*A*). The top half of the assembly is essentially a ring of 14 antiparallel α-helices in which helix H4 interacts with helix H2′ of the following protomer. Below this region, the helical interactions between adjacent protomers is more complex as helix H1 folds back to further stabilize the H4/H2′ interface. At the base of the assembly, it tapers into a seven helical parallel array involving the C-terminal ends of helix H4. There are no interactions between protomers A and G where the assembly opens up to form the helical array, although Phe133 at the C terminus of G packs into the H2/H4 interface of A to close off the base of the assembly (Fig. 3*B* and *SI Appendix*, Fig. S2). Similar to the protomer structure, the heptameric assembly is stabilized by five strategically placed and conserved salt bridges, Glu4:Lys44′, Glu79:Lys80′, Glu82:Arg67′, Asp97:Lys54′, and Asp108:Lys43′. The Glu79:Lys80′ and Glu82:Arg67′ salt bridges, together

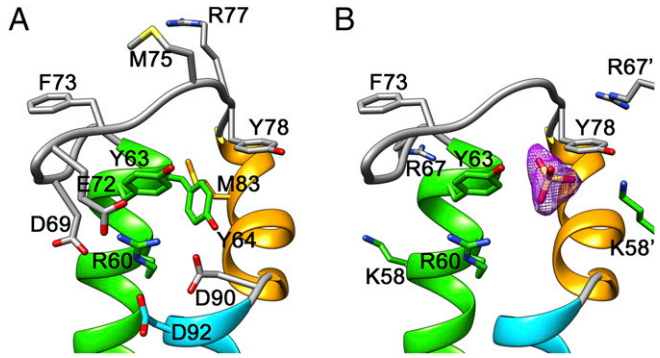

Fig. 2. Structure of the UvsY L2/H3 subdomain. (*A*) Key residues involved in stabilizing the local fold of the subdomain and mediating the head-to-head crystal packing of UvsY heptamers. (*B*) Locations of the six residues within the subdomain that were used to probe the interaction of UvsY with ssDNA. The purple electron density is from an mFo-DFc map contoured at the 5σ level. It is present in each protomer of the heptameric assembly and consistent with a bound sulfate ion that may occupy an ssDNA phosphate binding site adjacent to Tyr63. Note that residues K58′ and R67′ are from the adjacent protomer within the heptamer. The structure is from the type 1 crystal form.

with an interaction between Tyr78 and Lys58′, link adjacent L2/H3 substructures. It is notable that the acidic amino acids within the salt bridge pairs all reside on one protomer, whereas their basic partners reside on the next protomer in the assembly (Fig. 1*C*). The adjacent L2/H3 substructures create a platform along the top rim of the assembly (Fig. 3*A*), and mutagenesis studies suggest that this is the binding locale for ssDNA (25). A persistent electron density peak adjacent to the OH group of Tyr63 below loop L2 refined as a sulfate ion in the type 1 crystal, and this may be the binding site of an ssDNA phosphate group (Fig. 2*B*).

Interaction of UvsY with ssDNA and gp32. To investigate how UvsY dynamically interacts with ssDNA and the ssDNA/gp32 assembly, we developed an in vitro assembly assay by using SPR (*SI Appendix*, Fig. S5 *A* and *B*). We first verified that UvsY binds robustly to the captured dT60 oligonucleotide (*SI Appendix*, Fig. S5*C*) and that our assay is capable of reproducing the known interactions with gp32 (Fig. 4*A*). We also confirmed that the N-terminal and C-terminal subdomains of gp32 are necessary for homomeric and heteromeric interactions, respectively. Thus, gp32ΔC (missing residues 240–301) binds ssDNA almost as well as full-length gp32 but fails to generate the ssDNA–gp32–UvsY ternary complex (Fig. 4*B*). Conversely, gp32ΔN (missing residues 1–21) is compromised in binding ssDNA but still able to generate the ternary complex (Fig. 4*C*). We then generated six UvsY point mutations within the L2/H3 substructure that would be predicted to disrupt the proposed ssDNA-binding surface and compromise the ssDNA–UvsY complex (Figs. 1*A* and 2*B*). These mutants showed reduced binding to ssDNA compared with the wild type apart from R60A that is close to wild type. All of the mutants were compromised in generating the ssDNA–gp32-UvsY ternary complex with R60A again showing the least deficiency (Fig. 5 and *SI Appendix*, Fig. S5 *D–I*). The only anomaly in these data related to F73A that generated a robust ternary complex despite binding poorly to ssDNA.

We then investigated the thermodynamics of the ssDNA–UvsY interaction by using ITC. We first analyzed the effect of ssDNA length on UvsY binding, and tested 4-mers to 28-mers in length increments of 2 nt (Table 1 and *SI Appendix*, Table S3 and Fig. S6). The data revealed four important features of the ssDNA–UvsY interaction. First, binding requires a minimum of 6 nt. Second, the ssDNA:UvsY stoichiometry of binding (or "N-value") remains one oligonucleotide per UvsY heptamer up to 20 nt. Third, the shapes of the binding isotherms for nucleotides up to 18 in length are similar and consistent with a one-site binding model, whereas the shapes clearly change beyond 18 and follow a two-site binding model. Inspection of the binding parameters reveals that the initial mode of binding is characterized by a relatively low affinity, a large release of heat, and a steadily increasing entropic penalty and a steadily decreasing K_d with increasing oligonucleotide length. This binding mode is consistent with electrostatic binding of the ssDNA backbone in which increasing heat is released and increasing ordering takes place as the oligonucleotide increases in length. In contrast, the second binding mode is more hydrophobic in nature and is characterized by a high affinity, a smaller release of heat, and a marginally favorable change in entropy. Finally, the N-value remains close to 1 during the one-site binding stage (nucleotides 6–18) but switches to ∼0.5 and ∼0.25 for the weak and strong sites, respectively, for longer oligonucleotides. The longest 28-mer oligonucleotide generates a ssDNA:UvsY binding stoichiometry of 1:2.

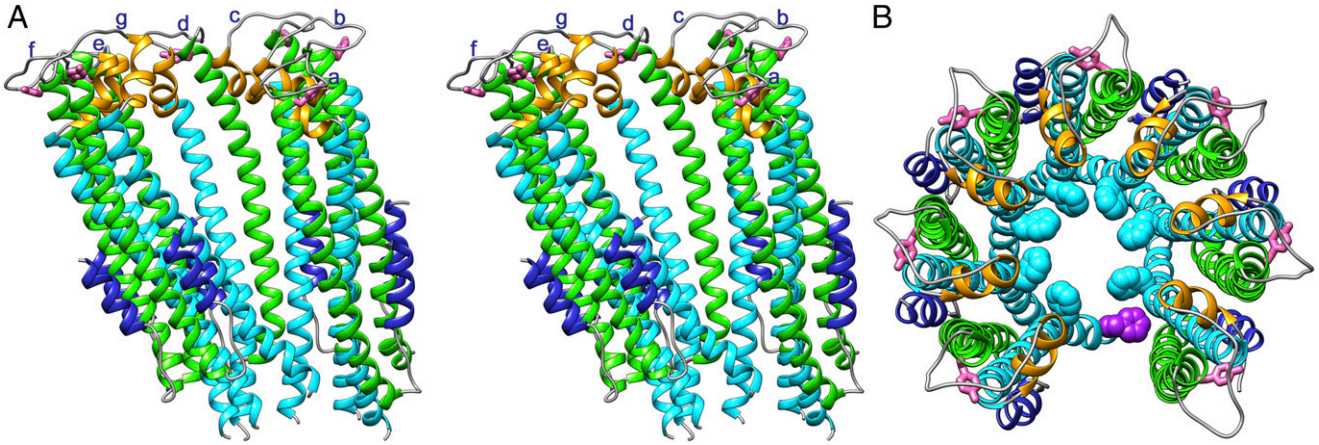

Fig. 3. The UvsY heptameric assembly. (*A*) Stereoview of the side of the assembly showing the opening between protomers A and G that creates the open barrel arrangement. Tyr63 from each protomer (in pink stick representation) is part of the proposed ssDNA-binding channel at the base of the L2/H3 subdomain. The type 2, type 3, and type 4 heptameric assemblies are shown in *SI Appendix*, Fig. S2. (*B*) View from the top of the assembly showing the array of L2/H3 subdomains and the tightly packed Phe122 residues from each protomer (in sky blue space filling representation) at the base of the inner surface. Tyr63 again shows the suggested ssDNA-binding channel. Also shown is the packing of Phe133 of chain G against chain A (purple space filling). *SI Appendix*, Fig. S2 shows this interaction as it occurs in all four of the independent UvsY structures.

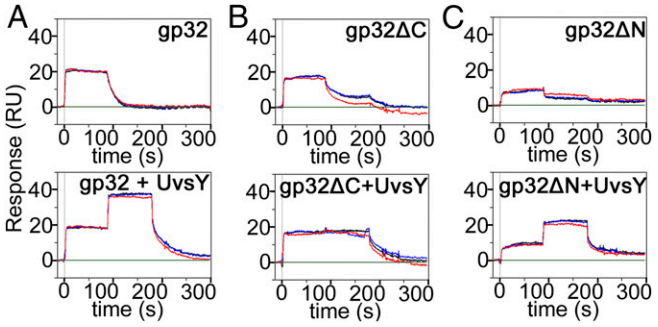

Fig. 4. SPR analyses of UvsY interactions with gp32. A schematic of the SPR experiments is shown in *SI Appendix*, Fig. S5. (*A*) Interactions of gp32 (*Top*) and gp32 followed by UvsY (*Bottom*) with dT60. (*B*) Interactions of gp32ΔC (*Top*) and gp32ΔC followed by UvsY (*Bottom*) with dT60. gp32ΔC lacks the C-terminal protein–protein interacting extension. (*C*) Interactions of gp32ΔN (*Top*) and gp32ΔN followed by UvsY (*Bottom*) with dT60. gp32ΔN lacks the N-terminal gp32–gp32 interacting extension. The black, blue, and red lines show three repetitions of the experiments.

Discussion

It has been proposed that the mechanism by which UvsY promotes HR involves wrapping the extended ssDNA–gp32 complex and, thereby, changing the architecture of ssDNA such that UvsX binding is preferred over gp32 binding (26). Our UvsY structural and biophysical data are fully compatible with this model. Most importantly, the helical UvsY assembly can generate the necessary "open" UvsX–ssDNA complex that is required to nucleate the helical HR filament rather than a closed ring assembly where this is not possible. Using mutagenesis and SPR analyses, we also showed that the L2/H3 substructure is the likely ssDNA-binding region, specifically below loop L2 where there is electron density consistent with a bound sulfate ion. It has been estimated that UvsY engages 3–4 nt per protomer (14, 18, 26), and the protomer-protomer spacing in the region is 21 Å, consistent with 3–4 linearly bound nucleotides. SPR analyses also support earlier observations (15, 17, 27) that ssDNA, gp32, and UvsY can form a ternary complex that mediates the gp32/UvsX exchange, and we constructed a model of this putative complex (Fig. 6*A*). The model is based on the more open type 3 structure and demonstrates that the UvsY heptamer can indeed accommodate seven bound molecules of gp32 in a fashion that allows their simultaneous interaction with ssDNA.

Our ITC and SPR data provide additional key insights into the ssDNA–UvsY interaction. For nucleotide lengths of 6–20, there is only one binding event per heptamer and the stoichiometry of the complex remains close to 1. There is sufficient room on the heptamer to bind multiple short oligonucleotides, and the stoichiometry would be predicted to be ∼3 for the 6-mer and decrease to 1 with increasing length. This observation suggests that the UvsY assembly is asymmetric and that there is a preferred entry point for binding. We note that previous studies using AUC have reported that the UvsY assembly can bind multiple short oligonucleotides (26), but our ITC data are not consistent with this and the previous studies assumed that UvsY exists as a hexamer. As the oligonucleotide length approaches the value predicted to saturate the heptamer (20-mer), two binding modes begin to appear. One mode is similar to that observed with the shorter oligonucleotides and suggests a mainly electrostatic mode of binding. The second is much tighter and less electrostatic in nature, and is consistent with the longer oligonucleotide becoming locked into a tight complex via hydrophobic and/or van der Waals interactions. Within the open helical assembly, the protomers flanking the gap display two different surfaces that are possible candidates for the entry point and the second mode of binding (Fig. 6*A*). The stoichiometry eventually shifts toward 2 with the longer oligonucleotides, which suggests that two UvsY heptamers can simultaneously engage the oligonucleotide when its length exceeds that required to saturate the assembly.

Previous studies have suggested that UvsY forms a hexamer (12), but our crystallographic analyses consistently reveal a heptameric open-barrel assembly of protomers that is supported by solution studies. The elongated α-helical structure of the UvsY protomer is well suited to create this barrel-like assembly. However, the helical pitch is quite variable and the type 4 structure would require only minor rearrangements to achieve a fully closed arrangement. The charge separation at the protomer interface (Fig. 1*C*) may play a role in these rearrangements. We therefore suggest that UvsY exists as a metastable closed barrel in solution that opens up when it engages the ssDNA–gp32 complex, similar to other systems (28). Two features of the more compressed structure suggest that a closed ring would be metastable: an increase in the positive charge in the center of the heptamer (*SI Appendix*, Fig. S7), and steric clash between the side chains of Phe122 at the base of the heptamer (Fig. 3*B* and *SI Appendix*, Fig. S2). The crystallization conditions all mimic a DNA-bound environment to some degree, which may explain why we only observe the open heptamer rings.

Our SPR data also support previous observations (17, 29) that the C terminus of gp32 is required for the recruitment of UvsY to the ternary complex. In our model of the ternary complex (Fig. 6*A*), the gp32 proteins are arrayed such that the flexible C termini can engage the outer surface of the UvsY heptamer. Such an interaction would have to be relatively nonspecific to explain how the gp32 C terminus is able to recruit other T4 proteins such as UvsX, UvsW, Dda, and DNA polymerase (30, 31). Shown in Fig. 6 *B*–*D* is a model for how the proposed ternary complex is created and then mediates the formation of the UvsX recombination filament. In this model, UvsY is initially an unbound heptamer that opens to create the ssDNA entry site and then engages ssDNA–gp32 complex. The ssDNA–gp32 interactions are weakened by the loss of the gp32–gp32 cooperative interactions, and this loss allows UvsX to replace gp32 in a ssDNA-UvsY-UvsX ternary complex that acts to nucleate the UvsX filament. Phe73 within loop L2 adopts different conformations in our crystal structures and may have an important role in this model. It apparently interacts with ssDNA in the ssDNA–UvsY binary complex but not in the ternary complex with gp32 (Fig. 5*C*).

Our studies support the notion that the core T4 HR machinery comprising UvsX, UvsY, and UvsW functions in the same manner

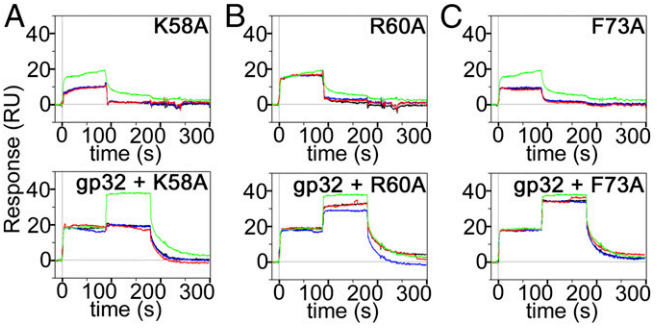

Fig. 5. SPR analyses of the interactions between three selected UvsY point mutants with ssDNA and gp32. The black, blue, and red lines show three repetitions of the experiments with mutant UvsY, and the green line shows the UvsY wild-type experiment for comparison. Top graphs show how the three mutants interact with dT60, and the bottom graphs show how each mutant interacts with the preformed gp32–dT60 complex. The same SPR chip was used in all experiments. (*A*) The K58A mutant has reduced binding to ssDNA and does not form a ternary complex with gp32. The Y63A, R67A, and Y78A mutants showed similar binding behaviors (*SI Appendix*, Fig. S5). (*B*) The R60A mutant shows similar binding as wild-type UvsY. (*C*) The F73A mutant shows weak binding to ssDNA but is competent in forming the ternary ssDNA–gp32–UvsY complex.

Table 1. Thermodynamic quantities obtained from isothermal titration calorimetry analyses of UvsY–ssDNA interactions

Oligo	K_d, μM	Δ*G*, kcal/mol	Δ*H*, kcal/mol	-TΔ*S*, kcal/mol	*N*
dT6	1.58	−7.92	−12.65	4.72	0.95
dT8	2.08	−7.77	−12.11	4.33	0.96
dT10	2.27	−7.71	−11.67	3.95	0.95
dT12	1.0	−8.19	−12.55	4.35	0.96
dT14	0.62	−8.49	−13.33	4.83	0.93
dT16	0.20	−9.14	−14.34	5.19	1.00
dT18	0.14	−9.36	−16.78	7.41	0.96
dC20–first	0.13	−9.39	−25.18	17.78	0.80
dC20–second	0.016	−10.65	−18.58	7.84	0.33
dT20–first	0.17	−9.25	−25.43	16.18	0.60
dT20–second	0.018	−10.58	−13.31	2.72	0.23
dT22–first	0.19	−9.18	−21.18	11.99	0.53
dT22–second	0.044	−10.07	−8.34	−0.84	0.30
dT24–first	0.16	−9.30	−24.0	14.69	0.50
dT24–second	0.040	−10.11	−8.94	−1.16	0.30
dT26–first	0.20	−9.14	−24.5	15.36	0.50
dT26–second	0.025	−10.40	−7.93	−2.46	0.20
dT28–first	0.18	−9.20	−33.95	24.75	0.30
dT28–second	0.022	−10.48	−13.85	3.37	0.20

Oligonucleotides up to 18 nt in length could be fitted by a one-site binding model. Longer oligonucleotides required a two-site binding model (first and second). See *SI Appendix*, Fig. S5 for representative binding isotherms and data fitting, and *SI Appendix*, Table S3 for the SDs from triplicate measurements.

as the eukaryotic machinery comprising Rad51, Rad52, and Rad54. It is well known that the T4 DNA metabolic proteins are generally more similar to those of eukaryotes than prokaryotes (32–34), and our previous studies have confirmed the structural similarities of UvsX/Rad51 and UvsW/Rad54 (11, 20). It is therefore surprising that UvsY and Rad51 share no apparent sequence or structural similarities. However, full-length Rad52 has been reported to form a heptamer similar to UvsY (35, 36), and it also contains a similar putative ssDNA-binding groove, albeit in the context of an undecameric complex formed by a truncated construct (35, 37). UvsY and Rad52 also form similar ternary complexes (38). UvsY and Rad52 therefore appear to have evolved by convergent evolution. We have demonstrated that, although T4 HR performed in vitro does not require UvsY, it is more efficient when present (11). This observation may explain why it apparently appeared later in evolution. Unlike UvsY, the Rad52 heptamer and undecamer are both closed rings that cannot obviously nucleate the helical HR filament. This observation supports the notion that isolated UvsY forms a closed ring and also that Rad52 forms a UvsY-like open structure when functional. We speculate that the heptameric assembly is dictated by the need to form one turn of an extended locked 6_1 helix in the ssDNA–UvsY–UvsX and ssDNA–Rad52–Rad51 ternary complexes to nucleate the approximate 6_1 helix in the growing HR filament.

Experimental Procedures

Detailed experimental procedures are available in *SI Appendix, Experimental Procedures*.

Proteins and Oligonucleotides. UvsY and gp32 protein samples were obtained by expression in *E. coli*. UvsY was expressed in two forms, with and without a 6xHis fusion tag. Tagged UvsY was used to generate the type 1, type 2, and type 4 crystals and for the SPR experiments. Untagged UvsY was used to generate the type 3 crystals and for the ITC, AUC, and SEC-MALS experiments. Gp32 was expressed and purified with a 6xHis fusion tag. Oligonucleotides of lengths ranging from 4-mers to 28-mers for ITC were purchased from Integrated DNA Technologies, and 5′ biotinylated oligonucleotides for SPR were purchased from Sigma Aldrich.

Crystallographic Analyses. Four crystal forms of UvsY were used in these studies. Types 1, 2, and 4 were grown from UvsY that had undergone reductive methylation (22). In the type 4 crystals, residues 79–81 were also mutated to alanines according to entropy reduction predictions (39). Type 3 crystals were grown from unmodified UvsY in the presence of dA3 oligonucleotide. All crystals were cryoprotected and flash frozen before data collection. Data were processed by using XDS (40) or HKL2000 (41), and anisotropic data were truncated and scaled with the University of California, Los Angeles anisotropy diffraction server (42). The type 2 structure was first determined by using selenium SAD methods, and the types 1, 3, and 4 structures were subsequently determined by molecular replacement (MR) using the type 2 structure as search model. The type 2 electron density map was initially determined to 5.4 Å by using a combination of SHELX (43) and Phaser (44), and improved by using RESOLVE (45) and CNS (46). Map interpretation was achieved by using BCL::EM_Fold (23) and Rosetta (24), and the model was refined by using phenix.refine (47). The type 1 structure was initially determined by using a dataset processed as triclinic, and the true space group was identified as $C222_1$ with pseudo merohedral twinning by using the *Zanuda* program (48). Molecular graphics procedures were performed with the UCSF Chimera package (49) from the Computer Graphics Laboratory, University of California, San Francisco (supported by NIH Grant P41 RR-01081).

AUC. Experiments were conducted by using a ProteomeLab XL-I analytical ultracentrifuge (Beckman Coulter) following standard protocols (50), and data were modeled by using SEDFIT and SEDPHAT (https://sedfitsedphat.nibib.nih.gov/software/default.aspx).

SEC-MALS. Experiments were performed by using a Showdex PROTEIN KW-803 size-exclusion column (SHOWA DENKO) with three detectors connected in series: an Agilent 1200 UV detector (Agilent Technologies), a Wyatt DAWN-HELEOS MALS, and a Wyatt Optilab rEX differential refractive index detector (Wyatt Technologies). Data were recorded and analyzed with the Wyatt Astra software (version 6.0.5.3) and plotted as a molar mass distribution superimposed on the elution profile (51).

SPR. Experiments were conducted at 25 °C by using a Biacore 3000 optical biosensor (GE Healthcare). Streptavidin (Thermo Scientific) was covalently

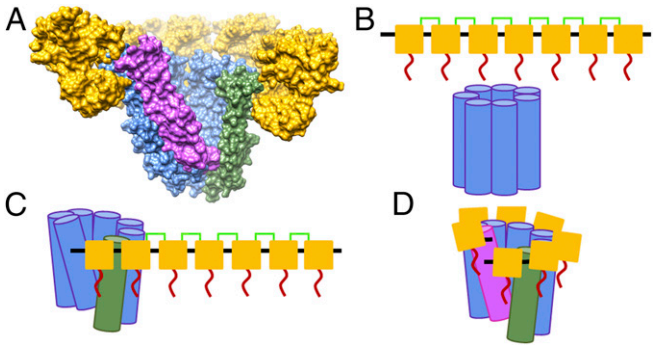

Fig. 6. A model for how the putative heptameric ssDNA–gp32–UvsY ternary complex is formed. (*A*) The final ternary complex structure. Seven gp32 molecules (yellow) lacking the N- and C-terminal extensions (PDB ID code 1GPC) engage the UvsY L2/H3 subdomains such their proposed ssDNA-binding surfaces can "share" the bound ssDNA (not modeled). UvsY protomers are blue apart from the green and purple protomers that flank the gap and are proposed to create the ssDNA entry point and the ssDNA tight binding site. In this model, the flexible gp32 C terminus is able to bind on the helical exterior of the assembly. (*B–D*) A schematic of how the ternary complex is formed using the same colors as (*A*). ssDNA is shown in black, the gp32 C terminus is shown in red, and the gp32–gp32 cooperative interactions mediated by the N terminus are show as light green. (*B*) gp32 binds linear ssDNA tightly via cooperative interactions, and unbound UvsY potentially exists as a closed heptameric ring. (*C*) The binding of ssDNA creates the green entry site on the UvsY heptamer as the ring opens. (*D*) The ssDNA-gp32 array engages the open UvsY heptamer with the ssDNA at the interface. The gp32–gp32 interactions are lost as the ternary complex is formed, and the gp32 C-termini engage the outer surface of the heptamer. The binding of the final gp32 molecule creates the tight UvsY-binding site (purple).

immobilized on a carboxylated gold surface (C1 chip; GE Healthcare), and biotinylated ssDNA60 was subsequently captured by injection. Various combinations of gp32 and UvsY were then injected, followed by buffer to observe the dissociation of the complexes. Data were also collected on a reference cell containing streptavidin with no captured DNA. The data were processed and double-referenced (52) by using the software package Scrubber 2 (version 2.0c; BioLogic Software).

ITC. Thermodynamic parameters were measured by using a MicroCal auto-iTC 200 (GE Healthcare). Results were analyzed by using Origin software (OriginLab) provided by MicroCal. Binding constants (K_d) and thermodynamic parameters were calculated from the average of three individual titrations by fitting the data to a one-site or two-site binding model by using a nonlinear least-squares fitting algorithm.

ACKNOWLEDGMENTS. We thank Kenneth Kreuzer for his long-term support of this project and his invaluable insights and suggestions; Eric Enemark, Darcie Miller, John Bollinger, Jürgen Bosch, and Randy Read for their helpful comments on the crystallography; and Sheila Chriswell and Xiaoping He for helping to prepare the protein samples. The majority of the diffraction data were collected at Southeast Regional Collaborative Access Team (SERCAT) beam lines 22-ID and 22-BM at the Advanced Photon Source, Argonne National Laboratory, and we thank SERCAT staff for their assistance. Supporting SERCAT institutions may be found at www.ser-cat.org/members.html. Use of the Advanced Photon Source was supported by the US Department of Energy under Contract W-31-109-Eng-38. Additional data were collected at the ALS 822 beam line facility. Work in the S.W.W. laboratory is supported by NIH Grant GM066934, Cancer Center core Grant CA21765, and the American Lebanese Syrian Associated Charities. Work in the J.M. laboratory is supported by NIH Grants GM080403, GM099842, DK097376, HL122010, GM073151, and AI117905, and by National Science Foundation Grant CHE 1305874.

1. Krejci L, Altmannova V, Spirek M, Zhao X (2012) Homologous recombination and its regulation. *Nucleic Acids Res* 40(13):5795–5818.
2. San Filippo J, Sung P, Klein H (2008) Mechanism of eukaryotic homologous recombination. *Annu Rev Biochem* 77:229–257.
3. Sung P, Krejci L, Van Komen S, Sehorn MG (2003) Rad51 recombinase and recombination mediators. *J Biol Chem* 278(44):42729–42732.
4. Chen Z, Yang H, Pavletich NP (2008) Mechanism of homologous recombination from the RecA-ssDNA/dsDNA structures. *Nature* 453(7194):489–494.
5. Bell JC, Plank JL, Dombrowski CC, Kowalczykowski SC (2012) Direct imaging of RecA nucleation and growth on single molecules of SSB-coated ssDNA. *Nature* 491(7423): 274–278.
6. Galletto R, Amitani I, Baskin RJ, Kowalczykowski SC (2006) Direct observation of individual RecA filaments assembling on single DNA molecules. *Nature* 443(7113): 875–878.
7. Beernink HT, Morrical SW (1999) RMPs: Recombination/replication mediator proteins. *Trends Biochem Sci* 24(10):385–389.
8. Wachsman JT, Drake JW (1987) A new epistasis group for the repair of DNA damage in bacteriophage T4: Replication repair. *Genetics* 115(3):405–417.
9. Chase JW, Williams KR (1986) Single-stranded DNA binding proteins required for DNA replication. *Annu Rev Biochem* 55:103–136.
10. Shamoo Y, Friedman AM, Parsons MR, Konigsberg WH, Steitz TA (1995) Crystal structure of a replication fork single-stranded DNA binding protein (T4 gp32) complexed to DNA. *Nature* 376(6538):362–366.
11. Gajewski S, et al. (2011) Crystal structure of the phage T4 recombinase UvsX and its functional interaction with the T4 SF2 helicase UvsW. *J Mol Biol* 405(1):65–76.
12. Beernink HT, Morrical SW (1998) The uvsY recombination protein of bacteriophage T4 forms hexamers in the presence and absence of single-stranded DNA. *Biochemistry* 37(16):5673–5681.
13. Hashimoto K, Yonesaki T (1991) The characterization of a complex of three bacteriophage T4 recombination proteins, uvsX protein, uvsY protein, and gene 32 protein, on single-stranded DNA. *J Biol Chem* 266(8):4883–4888.
14. Kodadek T, Gan DC, Stemke-Hale K (1989) The phage T4 uvs Y recombination protein stabilizes presynaptic filaments. *J Biol Chem* 264(28):16451–16457.
15. Sweezy MA, Morrical SW (1999) Biochemical interactions within a ternary complex of the bacteriophage T4 recombination proteins uvsY and gp32 bound to single-stranded DNA. *Biochemistry* 38(3):936–944.
16. Ando RA, Morrical SW (1998) Single-stranded DNA binding properties of the UvsX recombinase of bacteriophage T4: Binding parameters and effects of nucleotides. *J Mol Biol* 283(4):785–796.
17. Jiang H, Giedroc D, Kodadek T (1993) The role of protein-protein interactions in the assembly of the presynaptic filament for T4 homologous recombination. *J Biol Chem* 268(11):7904–7911.
18. Sweezy MA, Morrical SW (1997) Single-stranded DNA binding properties of the uvsY recombination protein of bacteriophage T4. *J Mol Biol* 266(5):927–938.
19. Melamede RJ, Wallace SS (1977) Properties of the nonlethal recombinational repair x and y mutants of bacteriophage T4. II. DNA synthesis. *J Virol* 24(1):28–40.
20. Kerr ID, et al. (2007) Crystallographic and NMR analyses of UvsW and UvsW.1 from bacteriophage T4. *J Biol Chem* 282(47):34392–34400.
21. Xu H, Beernink HT, Rould MA, Morrical SW (2006) Crystallization and preliminary X-ray analysis of bacteriophage T4 UvsY recombination mediator protein. *Acta Crystallogr Sect F Struct Biol Cryst Commun* 62(Pt 10):1013–1015.
22. Rypniewski WR, Holden HM, Rayment I (1993) Structural consequences of reductive methylation of lysine residues in hen egg white lysozyme: An X-ray analysis at 1.8-A resolution. *Biochemistry* 32(37):9851–9858.
23. Lindert S, et al. (2012) EM-fold: De novo atomic-detail protein structure determination from medium-resolution density maps. *Structure* 20(3):464–478.
24. Wang C, Bradley P, Baker D (2007) Protein-protein docking with backbone flexibility. *J Mol Biol* 373(2):503–519.
25. Bleuit JS, Ma Y, Munro J, Morrical SW (2004) Mutations in a conserved motif inhibit single-stranded DNA binding and recombination mediator activities of bacteriophage T4 UvsY protein. *J Biol Chem* 279(7):6077–6086.
26. Xu H, Beernink HT, Morrical SW (2010) DNA-binding properties of T4 UvsY recombination mediator protein: Polynucleotide wrapping promotes high-affinity binding to single-stranded DNA. *Nucleic Acids Res* 38(14):4821–4833.
27. Liu J, Qian N, Morrical SW (2006) Dynamics of bacteriophage T4 presynaptic filament assembly from extrinsic fluorescence measurements of Gp32-single-stranded DNA interactions. *J Biol Chem* 281(36):26308–26319.
28. Lyubimov AY, Costa A, Bleichert F, Botchan MR, Berger JM (2012) ATP-dependent conformational dynamics underlie the functional asymmetry of the replicative helicase from a minimalist eukaryote. *Proc Natl Acad Sci USA* 109(30):11999–12004.
29. Krassa KB, Green LS, Gold L (1991) Protein-protein interactions with the acidic COOH terminus of the single-stranded DNA-binding protein of the bacteriophage T4. *Proc Natl Acad Sci USA* 88(9):4010–4014.
30. Hurley JM, Chervitz SA, Jarvis TC, Singer BS, Gold L (1993) Assembly of the bacteriophage T4 replication machine requires the acidic carboxy terminus of gene 32 protein. *J Mol Biol* 229(2):398–418.
31. Perumal SK, Nelson SW, Benkovic SJ (2013) Interaction of T4 UvsW helicase and single-stranded DNA binding protein gp32 through its carboxy-terminal acidic tail. *J Mol Biol* 425(16):2823–2839.
32. Bernstein H, Bernstein C (1989) Bacteriophage T4 genetic homologies with bacteria and eucaryotes. *J Bacteriol* 171(5):2265–2270.
33. Spicer EK, et al. (1988) Primary structure of T4 DNA polymerase. Evolutionary relatedness to eucaryotic and other procaryotic DNA polymerases. *J Biol Chem* 263(16): 7478–7486.
34. Tsurimoto T, Stillman B (1990) Functions of replication factor C and proliferating-cell nuclear antigen: Functional similarity of DNA polymerase accessory proteins from human cells and bacteriophage T4. *Proc Natl Acad Sci USA* 87(3):1023–1027.
35. Kagawa W, et al. (2002) Crystal structure of the homologous-pairing domain from the human Rad52 recombinase in the undecameric form. *Mol Cell* 10(2):359–371.
36. Stasiak AZ, et al. (2000) The human Rad52 protein exists as a heptameric ring. *Curr Biol* 10(6):337–340.
37. Singleton MR, Wentzell LM, Liu Y, West SC, Wigley DB (2002) Structure of the single-strand annealing domain of human RAD52 protein. *Proc Natl Acad Sci USA* 99(21): 13492–13497.
38. Gibb B, et al. (2014) Protein dynamics during presynaptic-complex assembly on individual single-stranded DNA molecules. *Nat Struct Mol Biol* 21(10):893–900.
39. Goldschmidt L, Cooper DR, Derewenda ZS, Eisenberg D (2007) Toward rational protein crystallization: A Web server for the design of crystallizable protein variants. *Protein Sci* 16(8):1569–1576.
40. Kabsch W (2010) Xds. *Acta Crystallogr D Biol Crystallogr* 66(Pt 2):125–132.
41. Otwinowski Z, Minor W (1997) Processing of X-ray diffraction data collected in oscillation mode. *Methods Enzymol* 276:307–326.
42. Strong M, et al. (2006) Toward the structural genomics of complexes: Crystal structure of a PE/PPE protein complex from Mycobacterium tuberculosis. *Proc Natl Acad Sci USA* 103(21):8060–8065.
43. Sheldrick GM (2010) Experimental phasing with SHELXC/D/E: Combining chain tracing with density modification. *Acta Crystallogr D Biol Crystallogr* 66(Pt 4):479–485.
44. McCoy AJ, et al. (2007) Phaser crystallographic software. *J Appl Cryst* 40(Pt 4):658–674.
45. Terwilliger TC (2000) Maximum-likelihood density modification. *Acta Crystallogr D Biol Crystallogr* 56(Pt 8):965–972.
46. Brünger AT, et al. (1998) Crystallography & NMR system: A new software suite for macromolecular structure determination. *Acta Crystallogr D Biol Crystallogr* 54(Pt 5): 905–921.
47. Afonine PV, et al. (2012) Towards automated crystallographic structure refinement with phenix.refine. *Acta Crystallogr D Biol Crystallogr* 68(Pt 4):352–367.
48. Lebedev AA, Isupov MN (2014) Space-group and origin ambiguity in macromolecular structures with pseudo-symmetry and its treatment with the program Zanuda. *Acta Crystallogr D Biol Crystallogr* 70(Pt 9):2430–2443.
49. Pettersen EF, et al. (2004) UCSF Chimera–a visualization system for exploratory research and analysis. *J Comput Chem* 25(13):1605–1612.
50. Zhao H, et al. (2015) A multilaboratory comparison of calibration accuracy and the performance of external references in analytical ultracentrifugation. *PLoS One* 10(5): e0126420.
51. Kendrick BS, Kerwin BA, Chang BS, Philo JS (2001) Online size-exclusion high-performance liquid chromatography light scattering and differential refractometry methods to determine degree of polymer conjugation to proteins and protein-protein or protein-ligand association states. *Anal Biochem* 299(2):136–146.
52. Myszka DG (1999) Improving biosensor analysis. *J Mol Recognit* 12(5):279–284.